

# Orbital- and millennial-scale variability of the Antarctic Circumpolar Current over the past 140,000 years

**Shuzhuang Wu** (✉ [shuzhuang.wu@awi.de](mailto:shuzhuang.wu@awi.de))

Alfred-Wegener-Institut Helmholtz-Zentrum für Polar- und Meeresforschung <https://orcid.org/0000-0002-5134-8395>

**Lester Lembke-Jene**

Alfred-Wegener-Institut Helmholtz-Zentrum für Polar- und Meeresforschung <https://orcid.org/0000-0002-6873-8533>

**Frank Lamy**

Alfred Wegener Institute for Polar and Marine Research <https://orcid.org/0000-0001-5952-1765>

**Helge Arz**

Leibniz Institute for Baltic Sea Research <https://orcid.org/0000-0002-1997-1718>

**Norbert Nowaczyk**

Helmholtz Centre Potsdam, GFZ

**Wenshen Xiao**

Tongji University

**Xu Zhang**

Lanzhou University <https://orcid.org/0000-0003-1833-9689>

**H. Christian Hass**

Alfred Wegener Institute Helmholtz Centre for Polar and Marine Research

**Jürgen Titschack**

Marum

**Xufeng Zheng**

Key Laboratory of Marginal Sea Geology, South China Sea Institute of Oceanology, Chinese Academy of Sciences

**Jiabo Liu**

Southern University of Science and Technology

**Levin Dumm**

University of Bremen

**Bernhard Diekmann**

Alfred-Wegener-Institut Helmholtz-Zentrum für Polar- und Meeresforschung

**Dirk Nürnberg**

GEOMAR Helmholtz Centre for Ocean Research Kiel

**Ralf Tiedemann**

Alfred Wegener Institute for Polar and Marine Research

**Gerhard Kuhn**

Alfred Wegener Institute for Polar and Marine Research <https://orcid.org/0000-0001-6069-7485>

---

## Article

**Keywords:** Antarctic Circumpolar Current, ocean circulation, orbital-scale, millennial-scale

**Posted Date:** September 11th, 2020

**DOI:** <https://doi.org/10.21203/rs.3.rs-73426/v1>

**License:**   This work is licensed under a Creative Commons Attribution 4.0 International License.

[Read Full License](#)

---

**Version of Record:** A version of this preprint was published at Nature Communications on June 24th, 2021. See the published version at <https://doi.org/10.1038/s41467-021-24264-9>.

# Orbital- and millennial-scale variability of the Antarctic Circumpolar Current over the past 140,000 years

Shuzhuang Wu<sup>1\*</sup>, Lester Lembke-Jene<sup>1</sup>, Frank Lamy<sup>1</sup>, Helge W. Arz<sup>2</sup>, Norbert Nowaczyk<sup>3</sup>, Wenshen Xiao<sup>4</sup>, Xu Zhang<sup>1,5</sup>, H. Christian Hass<sup>6</sup>, Jürgen Titschack<sup>7,8</sup>, Xufeng Zheng<sup>9</sup>, Jiabo Liu<sup>3,10</sup>, Levin Dumm<sup>7</sup>, Bernhard Diekmann<sup>11</sup>, Dirk Nürnberg<sup>12</sup>, Ralf Tiedemann<sup>1</sup>, Gerhard Kuhn<sup>1</sup>

<sup>1</sup>Alfred-Wegener-Institut Helmholtz-Zentrum für Meeres- und Polarforschung, 27568 Bremerhaven, Germany

<sup>2</sup>Leibniz Institute for Baltic Sea Research Warnemünde, 18119 Rostock, Germany

<sup>3</sup>Helmholtz Centre Potsdam GFZ German Research Centre for Geosciences, 14473 Potsdam, Germany

<sup>4</sup>State Key Laboratory of Marine Geology, Tongji University, Shanghai 200092, China

<sup>5</sup>College of Earth and Environmental Sciences, Lanzhou University, 730000 Lanzhou, China

<sup>6</sup>Alfred-Wegener-Institut Helmholtz-Zentrum für Meeres- und Polarforschung, 25980 Sylt, Germany

<sup>7</sup>MARUM–Center for Marine Environmental Sciences, University of Bremen, 28359 Bremen, Germany

<sup>8</sup>Senckenberg am Meer, Marine Research Department, 26382 Wilhelmshaven, Germany

<sup>9</sup>Key Laboratory of Marginal Sea Geology, South China Sea Institute of Oceanology, Chinese Academy of Sciences, 510301 Guangzhou, China

<sup>10</sup>Southern University of Science and Technology, Department of Ocean Science and Engineering, 518055 Shenzhen, China

<sup>11</sup>Alfred-Wegener-Institut Helmholtz-Zentrum für Meeres- und Polarforschung, 14473 Potsdam, Germany

<sup>12</sup>GEOMAR, Helmholtz Centre for Ocean Research Kiel, 24148 Kiel, Germany

## Abstract

The Antarctic Circumpolar Current (ACC) plays a crucial role in global ocean circulation by fostering deep-water upwelling and formation of new water masses. On geological time-scales, ACC variations are poorly constrained beyond the last glacial. Here, we reconstruct changes in ACC strength in the central Drake Passage over the past 140,000 years, based on grain-size and geochemical characteristics. We found significant glacial-interglacial changes of ACC flow speed, with reduced ACC intensity during glacials and a more vigorous circulation in interglacials. Superimposed on these orbital-scale changes are high-amplitude millennial-scale fluctuations, with ACC strength maxima correlating with diatom-based Antarctic winter sea-ice minima, particularly during full glacial conditions. We hypothesize that the ACC is closely linked to Southern Hemisphere millennial-scale climate

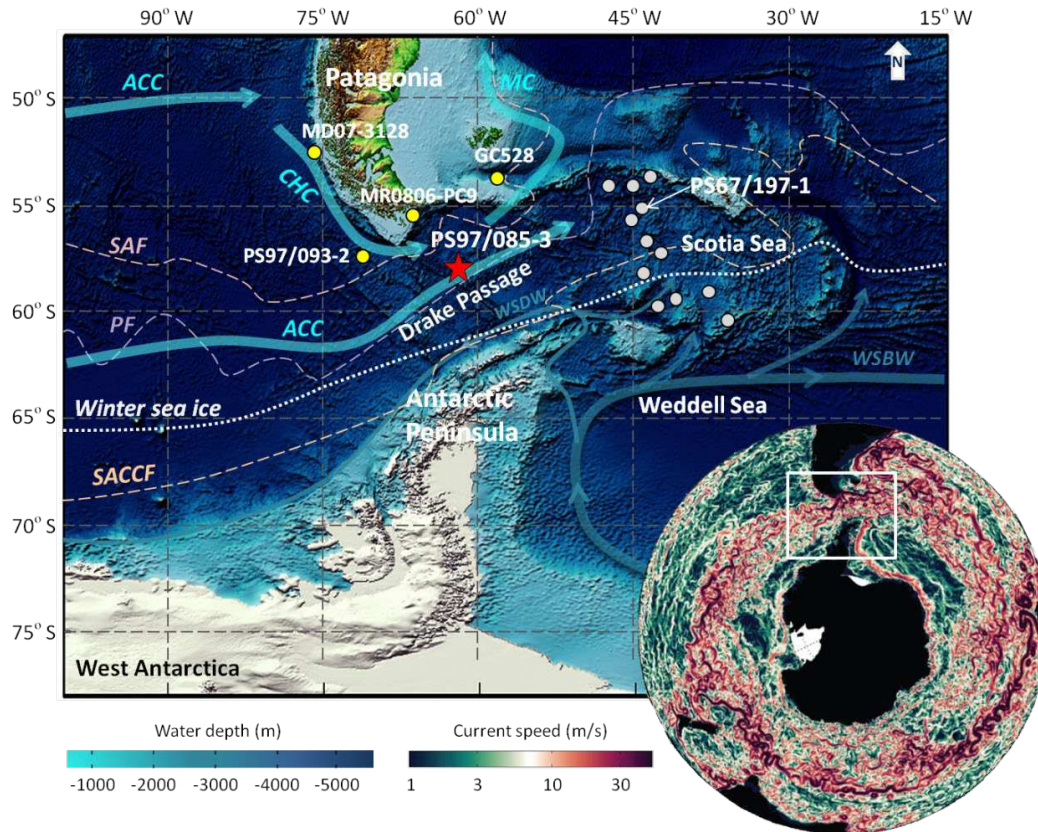
35 oscillations, amplified through Antarctic sea ice extent changes. These strong ACC  
36 variations regulated Pacific-Atlantic water exchange via the “cold water route” and  
37 affected the Atlantic Meridional Overturning Circulation and marine carbon storage.

38

39 The ACC is the strongest oceanic current system on Earth<sup>1</sup>. It represents the central  
40 distributor of globally important water masses, as it is intimately linked to the  
41 meridional overturning circulation cells of the adjoining Atlantic, Indian, and Pacific  
42 oceans. It bundles wind-driven surface circulation and thermohaline deep and bottom  
43 water circulation with impacts on global heat transport<sup>1,2</sup>. The configuration of its  
44 frontal systems with upwelling and downwelling cells is crucial for Antarctic climate,  
45 the modes of biological productivity and the physical and biological carbon pump<sup>3,4</sup>.  
46 Understanding the magnitude and sensitivity of the ACC during the geological past is  
47 crucial for assessing its role in the global MOC, in particular with regard to ongoing  
48 and future anthropogenic climate change. Proxy evidence for changes in ACC  
49 transport between the Pacific and Atlantic on glacial-interglacial timescales has  
50 yielded controversial results so far from locations both up- and downstream of the  
51 Drake Passage, with underlying forcing mechanism remaining largely elusive<sup>5-8</sup>. At  
52 present, the ACC strength is mainly driven by the southern westerly winds (SWW)  
53 and surface buoyancy forcing<sup>9,10</sup>. Previous studies proposed that sea ice cover, in  
54 addition to wind stress, has a significant influence on the surface ocean drag  
55 coefficient on forcing the ocean surface layer and ultimately current flow speed<sup>5,6,11</sup>.

56 The Drake Passage is the major “bottleneck” (Fig. 1) along the ACC path around  
57 Antarctica, subdivided by three oceanographic fronts: the Subantarctic Front (SAF),  
58 the PF, and the Southern ACC Front (SACCF)<sup>12</sup>. The ACC transports cold and fresh  
59 water from the Pacific to the Atlantic through the Drake Passage, known as “cold  
60 water route”<sup>13</sup>. This cold water route complements the warm westward Agulhas  
61 Current or “leakage” off the South African Cape of Good Hope known as “warm  
62 water route”. These two sources, together with deep waters originating from the  
63 Southern Ocean, comprise the northward-flowing return path balancing the  
64 AMOC<sup>1,13-16</sup>.

65 In this study, we reconstruct changes in Pacific-Atlantic ACC transport on  
66 millennial to glacial-interglacial time scales. We used high-resolution grain-size data  
67 of the siliciclastic sediment fraction and x-ray fluorescence (XRF) scanning-based  
68 elemental ratios from a sediment core in the central Drake Passage (Site PS97/085; 58°  
69 21.28' S, 62° 10.02' W; 3090 m water depth; Fig. 1) as bottom flow speed proxies.  
70 The age model is based on a combination of paleomagnetic excursions, relative  
71 paleointensity (RPI), radiocarbon dates, and tuning of high-resolution XRF  
72 scanning-derived calcium to titanium ratios ( $\ln(\text{Ca}/\text{Ti})$ ) to Antarctic temperature  
73 anomalies (see Supplementary methods; Table S1). Linear sedimentation rates range  
74 between ~2 and 40 cm/ka, with higher mass accumulation rates during full glacial  
75 periods (Fig. S3). In addition, we extend a previously published diatom-based winter  
76 sea ice record from the Scotia Sea further back in time to 60 ka (Site PS67/197, 55°  
77 8.24' S, 44° 6.28' W; 3837 m water depth; Fig. 1)<sup>17</sup>. The chronology of this latter  
78 core has been published before and is used here without modification<sup>18</sup>. Combining  
79 our ACC flow speed proxies with sea-ice reconstructions enables us to investigate  
80 millennial-scale ACC variations, potentially linked to Antarctic winter sea ice changes  
81 during the last glacial period.



82

83 **Fig. 1. Location map.** Core PS97/085-3 is located in the central Drake Passage (red star), ~20 nm  
 84 north of the Polar Front (see Supplementary Fig. S1). Yellow dots mark sediment cores in north of  
 85 the Subantarctic Front<sup>5,7,8</sup>. Grey dots indicate Scotia Sea transect cores south of the Polar Front<sup>6</sup>.  
 86 Core PS67/197-1 in the Scotia Sea is sensitive to changes in winter sea ice extent<sup>17</sup>. Light blue  
 87 arrows show the Antarctic Circumpolar Current (ACC), the Cape Horn Current (CHC)<sup>19</sup> and  
 88 Malvinas Current (MC)<sup>20</sup>, while dark green-blue arrows are Weddell Sea Bottom Water (WSBW,  
 89 thick) and Weddell Sea Deep Water (WSDW, thin) flows<sup>21</sup>. White dotted line is average modern  
 90 winter sea ice edge<sup>22</sup>. Dashed lines are the Subantarctic Front (SAF, pink), Polar Front (PF, purple)  
 91 and the Southern Antarctic Circumpolar Current Front (SACCF, orange)<sup>12</sup>. The right bottom insert  
 92 map shows study area inside the white box and current speed in the Southern Ocean, with warmer  
 93 red colors representing higher current speeds<sup>2</sup> adapted from Wu et al. (2019).

94

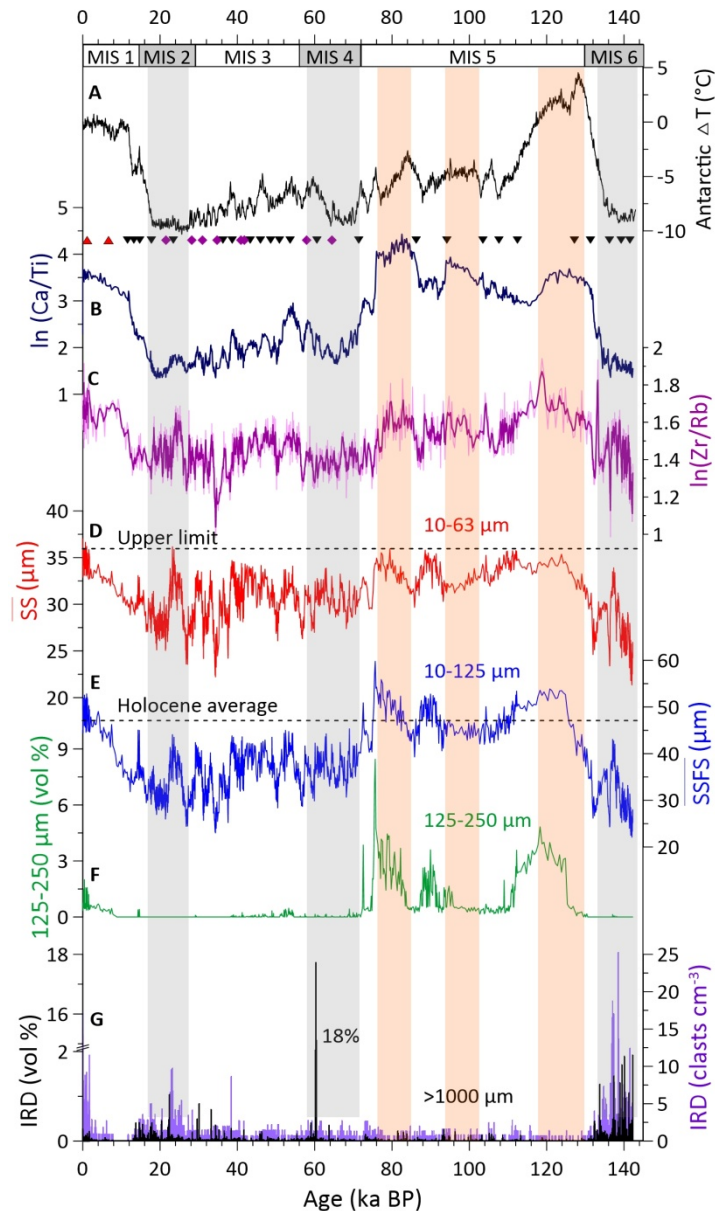
## 95 **Results and Discussion**

### 96 **ACC flow speed proxies for the Drake Passage**

97 We use changes in grain size and geochemical properties of the terrigenous sediment  
 98 fraction to reconstruct changes in ACC intensity (Fig. 2). The sortable silt mean grain  
 99 size ( $\overline{SS}$ , 10–63  $\mu\text{m}$ ) is typically applied for evaluating relative changes in the  
 100 near-bottom flow speed in deep-sea sediments<sup>23,24</sup>. We correlated near-bottom flow  
 101 speed mooring measurements with  $\overline{SS}$  of seafloor sediments on a north-south Drake  
 102 Passage transect<sup>25</sup>. However, modern observations reveal that ACC flow speeds are

103 frequently faster than 15 cm/s<sup>26</sup>; such high speeds can potentially remove parts of the  
104 silt and even the sand fractions<sup>23</sup>. The grain-size distribution mode would thus shift to  
105 the coarser fractions dominated by fine sand (Supplementary Fig. S4), and hence  
106 impair the  $\overline{SS}$  as a current speed proxy. Accordingly, the  $\overline{SS}$  may not capture the  
107 entire magnitude of the flow-speed variations in our record (Fig. 2D). High ACC  
108 speed can extend the sorting range beyond the sand-silt boundary (Supplementary Fig.  
109 S4), which was also observed at the Chilean Margin and the northernmost Drake  
110 Passage<sup>5</sup>. Therefore, we use the mean grain size of the sortable silt plus the fine sand  
111 fractions ( $\overline{SSFS}$ , 10-125  $\mu\text{m}$ ) as flow-speed proxy to reconstruct deep ACC dynamics  
112 throughout the past 140 ka (Fig. 2E). Since our site is  $\sim 250$  nm away from the South  
113 American continent, the terrigenous sand fractions are most likely transported by  
114 various processes (including sea ice, icebergs, etc.) from the continent and then  
115 reworked by bottom currents. Generally, unsorted ice-rafted debris (IRD) from glacial  
116 sources might affect the  $\overline{SS}$ -based flow speed proxy<sup>27</sup>. However, the content of IRD  
117 in our site samples is generally less than 2 vol.% and 20 clasts  $\text{cm}^{-3}$  (Fig. 2G). One  
118 spike with  $\sim 18$  vol.% at the end of Marine Isotope Stage (MIS) 4 might overestimate  
119 large clasts (see Supplementary methods). IRD fluctuations are overwhelmingly  
120 independent of  $\overline{SSFS}$  changes with short-term exceptions at 22-24 ka and in the  
121 oldest part beyond  $\sim 134$  ka (Supplementary Fig. S5). Furthermore, variations in  $\overline{SSFS}$   
122 and SSFS% component are positively correlated (Supplementary Fig. S5), suggesting  
123 bottom currents are the principal driver for changes in the grain-size fraction (10-125  
124  $\mu\text{m}$ ) at our site<sup>23,27</sup>.

125 Zirconium (Zr) is typically accumulating in the heavy mineral fraction associated  
126 with coarser grain sizes, while rubidium (Rb) is preferentially retained in the clay  
127 mineral fraction<sup>28</sup>. Previous studies found a positive correlation between grain size and  
128 the Zr/Rb ratio<sup>29,30</sup>. Therefore, the Zr/Rb ratios (Fig. 2C) can reflect changes in  
129 sediment fractions by current transport<sup>5,8</sup>, or aeolian input<sup>29</sup>. Major aeolian input can  
130 be ruled out in our study area by mineralogical and geochemical properties<sup>25,31,32</sup>.  
131 High-resolution records of grain size and Zr/Rb ratios can thus provide a robust  
132 signature of ACC variability.



133

134 **Fig. 2. Reconstructed changes in ACC intensity and compared with Southern Hemisphere**  
 135 **temperature signature.** A, Antarctic temperature changes from the European Project for Ice  
 136 Coring in Antarctica (EPICA) Dome C ice core<sup>33</sup>. B, High-resolution XRF scanner-derived  
 137 records of ln(Ca/Ti) (peak area count ratios) were applied to fine-tune to the Antarctic temperature  
 138 anomalies together with radiocarbon dates, relative paleo-intensity and paleomagnetic excursions  
 139 age control points from core PS97/085-3 (see Supplementary Methods, Fig. S2; S3). C,  
 140 XRF-derived Zr/Rb variations indicate changes in sediment grain-size fractions. D, Mean sortable  
 141 silt grain size ( $\overline{SS}$ , 10-63  $\mu\text{m}$ ) reaches up its limit under high flow speeds. E, Mean grain size of  
 142 sortable silt and fine sand ( $\overline{SSFS}$ , 10-125  $\mu\text{m}$ ) was used as the ACC strength proxy in this study. F,  
 143 Coarse sand fraction (125-250  $\mu\text{m}$ ), mainly in interglacials, inferring high current speeds  
 144 highlights the extension of the sorting effect to coarser grain sizes. G, Ice-rafted debris (IRD)  
 145 defined by larger than 1 mm grain size from X-ray computed topography scan (CT, see  
 146 Supplementary Methods). Vertical gray bars mark inferred glacial periods and pink bars inferred  
 147 the sub-interglacial during Marine Isotope Stage (MIS) 5.

## 148 **Changes in ACC strength in the central Drake Passage**

149 Our sediment record reveals glacial-interglacial variations in ACC flow speed in the  
150 central Drake Passage over the past 140 ka (Fig. 2). The timing of major ACC  
151 changes follows Antarctic temperature anomalies on orbital timescales<sup>34</sup>, implying the  
152 ACC strength in the Drake Passage is sensitive to Southern Hemisphere climate  
153 oscillations (Fig. 2A, C, E). The last interglacial (MIS 5e, ~129-116 ka) was warmer  
154 than today<sup>35</sup> with the average  $\overline{\text{SSF\text{S}}}$  value is ~49  $\mu\text{m}$ , while the Holocene average  
155 (~0-10 ka) occurred slightly smaller  $\overline{\text{SSF\text{S}}}$  with ~47  $\mu\text{m}$  (Fig. 2E). This suggests that  
156 the ACC flow speed during MIS 5e was slightly higher than during the present  
157 interglacial, supported by corresponding changes in Zr/Rb ratios (Fig. 2C). In contrast  
158 to MIS 5e and the Holocene, the ACC strength significantly decreased during the  
159 Penultimate Glacial Maximum (PGM, ~140 ka;  $\overline{\text{SSF\text{S}}} = \sim 28 \mu\text{m}$ ) and the Last  
160 Glacial Maximum (LGM, ~26-19 ka;  $\overline{\text{SSF\text{S}}} = \sim 34 \mu\text{m}$ ). The grain-size proxy  
161 records reveal a ~43% decrease in ACC strength during the PGM compared to MIS 5e,  
162 which is larger than the LGM to Holocene change of ~28%.

163 Our observed glacial reductions of the ACC flow speed in the central Drake  
164 Passage are broadly consistent with previous studies<sup>5,7,8</sup>. Various glacial-interglacial  
165 amplitudes of ACC changes were reported from the Drake Passage region<sup>5-8</sup>. Larger  
166 glacial-interglacial changes in flow speeds were observed north of the SAF with a  
167 range of ~20-50% (MD07-3128, MR0806-PC9 and GC528) at intermediate water  
168 depths (~600-1030 m)<sup>5,7</sup>. Smaller fluctuations in ACC changes (~10-16%, PS97/093-2)  
169 occurred in deep water (~3781 m) near the SAF<sup>8</sup>. In the central Drake Passage ~20  
170 nm north of the PF, the ACC throughflow exhibits a ~28-43% glacial reduction at  
171 ~3090 m water depth, which is considerably greater than variations along the Scotia  
172 Sea transect south of the PF ( $\leq 10\%$ , Scotia Sea transect cores, 2000-4300 m water  
173 depth)<sup>6</sup>. Differences between these results are likely due to the geographical settings  
174 within latitudinal subdivisions of the ACC and the related fronts. Therefore, we  
175 suggest an enhanced sensitivity of the ACC to glacial-interglacial climate changes  
176 around the PF and the SAF<sup>5,7,8</sup>, in contrast to minimal changes south of the PF along

177 the Scotia Sea transect<sup>6</sup>. Such presumption would be consistent with modern ACC  
178 transport and highest current velocities prevailing in the vicinity of the SAF and PF in  
179 the Drake Passage region<sup>26,36</sup>.

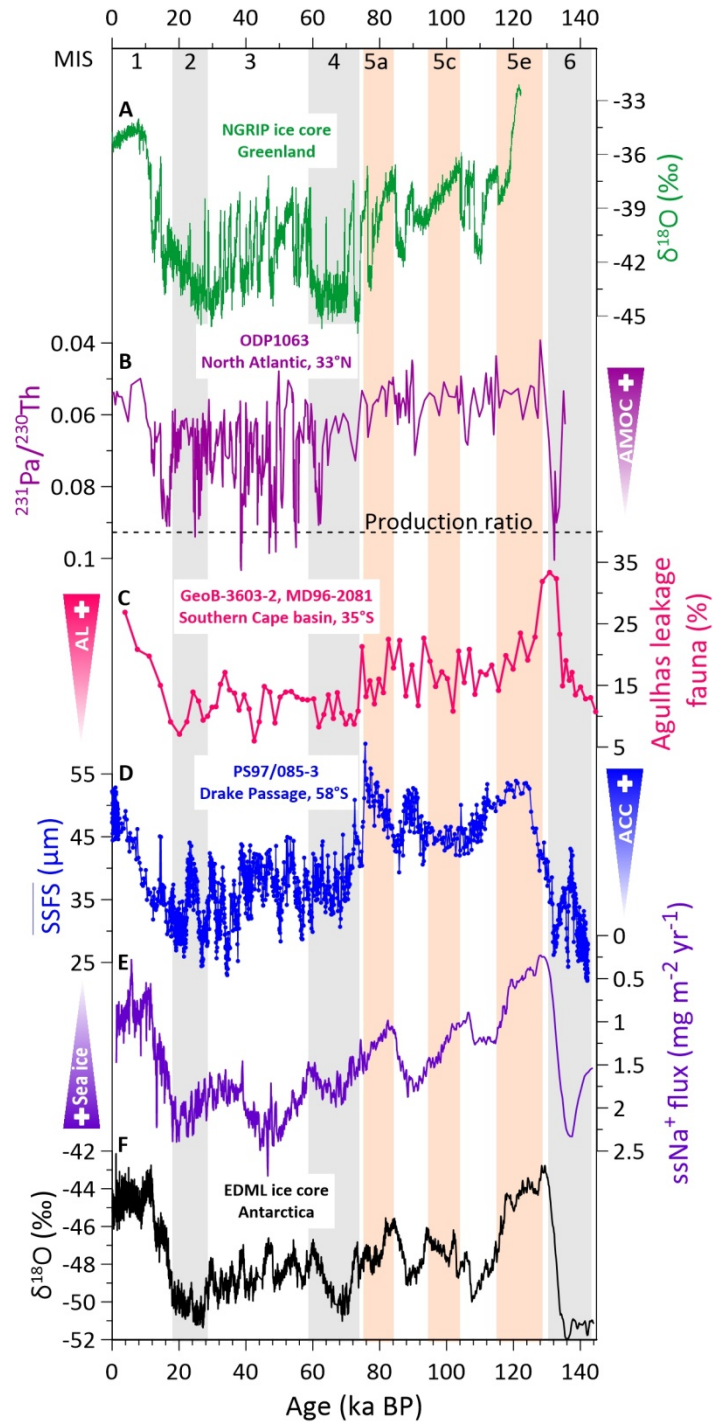
180 Several processes might cause these changes in the ACC strength at site  
181 PS97/085, including changes in the strength and latitudinal position of SWW<sup>9</sup>,  
182 oceanic fronts shift<sup>37</sup> and buoyancy forcing<sup>10</sup>. Although the intensity and position of  
183 the glacial SWW remain uncertain, a northward displacement of the SWW is widely  
184 assumed during the LGM<sup>38,39</sup>, with reduced impact on the ACC in the Drake Passage  
185 sector<sup>5,6,8</sup>. The glacial oceanic fronts were likewise suggested to have shifted  
186 equatorward<sup>37</sup>, thus the South American continent would have obstructed the ACC  
187 flow through the Drake Passage<sup>7</sup>. Moreover, changes in ACC strength on the  
188 glacial-interglacial timescale are corresponding to the sea salt sodium (ssNa) flux  
189 record from the East Antarctic Dronning Maud Land (EDML) ice core (Fig. 3D, E), a  
190 proxy partially related to large-scale sea ice production<sup>40,41</sup>. This indicates that major  
191 changes in circum-Antarctic sea ice cover might have been linked to  
192 glacial-interglacial ACC strength changes, in line with earlier suggestions<sup>5,6</sup>. During  
193 the LGM, seasonal sea ice likely expanded northward by more than ~500 km across  
194 the modern PF<sup>17,37,42,43</sup>. Such large sea ice coverage could have significantly  
195 decreased the efficiency of wind stress acting on the ocean surface<sup>5,6,11</sup> and thus  
196 reduced the ACC strength (Fig. 3D). Conversely, at interglacial stages, sea ice retreat  
197 and southward displacement of the SWW and oceanic fronts would have increased  
198 wind stress efficiency on the ocean surface and accelerated the ACC speed<sup>5,6,17</sup>.  
199 However, the sub-orbital ACC changes in our record are not evident in the ssNa flux  
200 pattern, e.g. during late MIS 5 and MIS 3 and 2 (Fig. 3D, E). We speculate that the  
201 ssNa flux in the EDML ice core may not have captured short-term regional changes in  
202 sea ice extent, but was influenced by changes in the hydrologic cycle as well<sup>40,44</sup>.

203

204 **Physical changes in the ACC linked to the AMOC stability**

205 Changes in ACC transport through the cold water route, together with the Agulhas  
206 leakage via the warm water route, have been suggested to regulate the AMOC  
207 strength<sup>5,15,16,45</sup>. However, the relative contribution of these two water routes for the  
208 upper branch of AMOC has rarely been addressed in the past. We compared our  
209 Drake Passage throughflow strength (Fig. 3D) with the Agulhas leakage intensity,  
210 reconstructed by planktic foraminiferal fauna census counts<sup>46</sup> in the South Africa  
211 margin over the past 140 ka (Fig. 3C). Both water routes' transport increased during  
212 the past two deglaciations<sup>46</sup> (Fig. 3C, D), suggesting that they both likely have  
213 induced a positive feedback to the AMOC recovering into a stronger interglacial mode  
214 as indicated by low  $^{231}\text{Pa}/^{230}\text{Th}$  ratios<sup>47-49</sup> (Fig. 3B).

215 The Agulhas leakage reached its transient transport maximum during the  
216 terminations, with subsequently significantly decreased water volume transport to the  
217 South Atlantic (~8 Sv during MIS 5) during interglacials<sup>50</sup>. In contrast, the Drake  
218 Passage throughflow remained strong throughout MIS 5, with smaller sub-interglacial  
219 fluctuations (Fig. 3D). Modern observations reveal the total mean ACC transport is  
220 between 130 and  $150 \pm 20$  Sv<sup>26,51</sup> and ~62% of subsurface water (50–1554 m, float  
221 depth) is flowing through the Drake Passage into the Malvinas Current<sup>20</sup>. Compared  
222 to modern conditions, we reconstructed higher ACC flow speeds during most of MIS  
223 5 (Fig. 3D), thus the ACC transport would have been larger than today. Such a  
224 stronger ACC might have enhanced the formation of surface and intermediate water to  
225 fuel the upper overturning cell in the Southern Ocean during MIS 5. In contrast to the  
226 lower Agulhas leakage transport, the cold water route may have played a crucial role  
227 in keeping the AMOC vigorous throughout MIS 5. A slow-down of the ACC at the  
228 MIS 5/4 transition, followed by high frequency variations through MIS 4 to MIS 2,  
229 might have been linked to higher AMOC instability<sup>47,48</sup> (Fig. 3B, D), while a sluggish  
230 Agulhas leakage prevailed during the last glacial period<sup>46</sup> (Fig. 3C). Although the  
231 ACC provided a dynamical link with the AMOC, several other important processes,  
232 like Southern Ocean wind-driven upwelling and buoyancy forcing<sup>45,52</sup>, may act  
233 together to explain the full changes of the AMOC.



234

235 **Fig. 3. Reconstructed changes in ACC strength compared with paleoclimatic records over**  
 236 **the past 140 ka.** A, Oxygen isotope record from North Greenland Ice Core Project (NGRIP,  $\delta^{18}\text{O}$   
 237 vs. VSMOW)<sup>53</sup>. B, Bermuda Rise  $^{231}\text{Pa}/^{230}\text{Th}$  data<sup>47-49</sup>, indicating the AMOC strength. Dashed  
 238 line is production ratio ( $^{231}\text{Pa}/^{230}\text{Th} = 0.093$ ), suggesting no transport. C, planktic foraminiferal  
 239 fauna reflect the intensity of the Agulhas leakage<sup>46</sup>. D,  $\overline{\text{SSFS}}$  as a flow-speed proxy for the ACC  
 240 strength (blue, this study). E, Sea salt sodium (ssNa) flux from EPICA Dronning Maud Land  
 241 (EDML) ice core, a proxy for sea ice, smoothed with a three-points running mean<sup>40</sup>. F, Oxygen  
 242 isotope record from the EDML ice core<sup>54</sup>. Vertical gray bars mark glacial periods and pink bars  
 243 mark the warm stages during MIS 5.

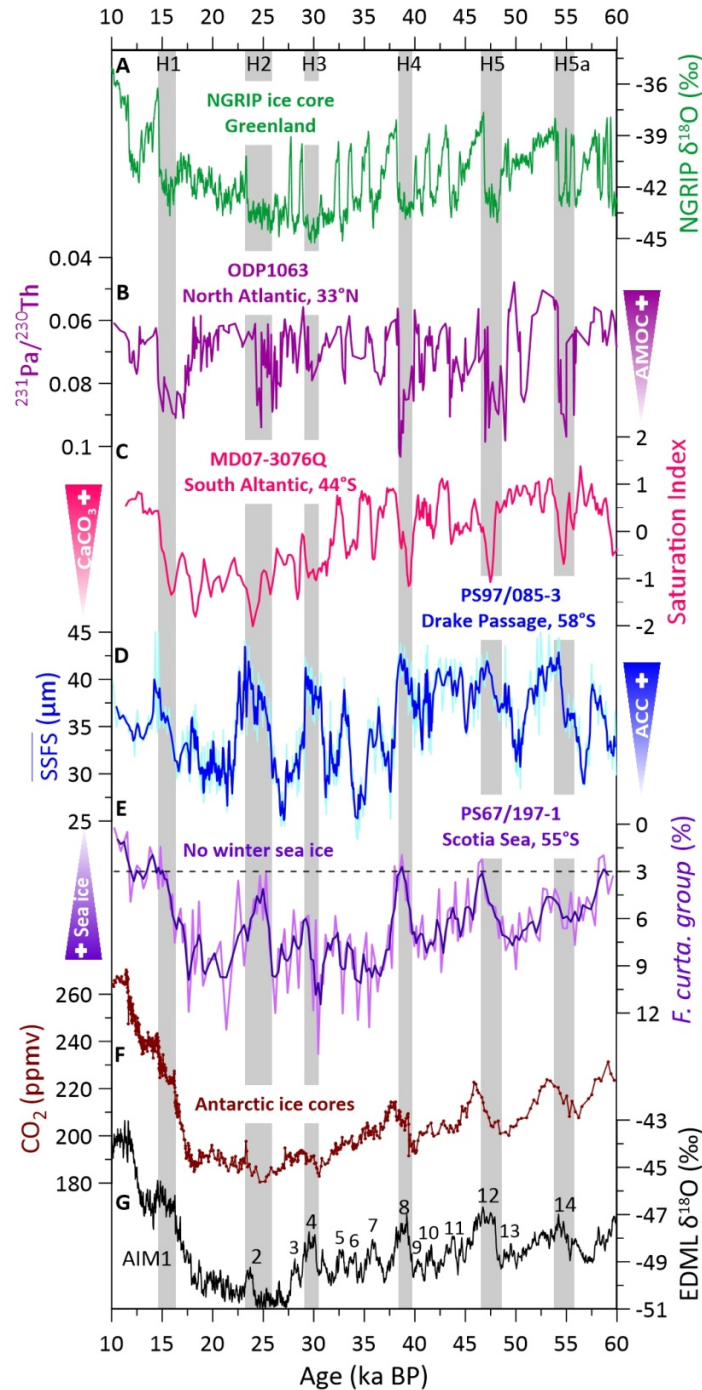
## 244 **Millennial-scale variations of ACC during the last glacial**

245 Superimposed on the glacial-interglacial changes, our records exhibit marked  
246 high-amplitude, millennial-scale variations in the ACC flow speeds covering the last  
247 glacial cycle with highest amplitudes between MIS 4 and MIS 2 (Fig. 4D). Overall, a  
248 stronger ACC coincides with a weakened AMOC during cold phases in the Northern  
249 Hemisphere and warm intervals in the Southern Hemisphere (Fig. 4A, B, D). We  
250 found increasing amplitudes of ACC millennial-scale variations as the climate was  
251 approaching the LGM (~38-23 ka; Fig. 4D), in contrast to a steady decline of the  
252 Antarctic temperatures (Fig. 4G). Enhanced sensitivity of the ACC towards the LGM  
253 was also recorded in the variation of the fine sand fraction percentages in the northern  
254 ACC/Cape Horn Current<sup>5</sup> (Supplementary Fig. S7). This suggests the ACC reached  
255 its highest sensitivity to Southern Hemisphere millennial-scale climate oscillations  
256 during full glacial conditions, with the ACC re-accelerating to higher flow speeds  
257 during Antarctic warming events associated with Northern Hemisphere Heinrich  
258 Stadials<sup>55</sup>.

259 Supporting evidence for causes of millennial-scale ACC strength changes near  
260 our site is scarce. While regional temperature proxy records from Antarctica<sup>33</sup> and off  
261 southernmost South America<sup>7,56</sup> show some correspondence to our ACC strength  
262 reconstruction, remaining dissimilarities indicate that factors other than temperature  
263 changes played a role in forcing ACC flow variations. Previous ACC strength  
264 reconstructions from sites north of our location attributed variations to SWW<sup>5</sup>  
265 changes and according northward shifts of the SAF<sup>7</sup>. However, model simulations of  
266 millennial-scale SWW changes indicate relatively small-scale variations during  
267 glacial periods<sup>57</sup>, which alone may have been insufficient to drive high-amplitude  
268 changes in ACC speeds from surface to 3090 m water depth (Fig. 4D). We thus chose  
269 to investigate potential regional amplification effects of sea ice changes on  
270 millennial-scale ACC dynamics, as the EDML ssNa flux did not indicate  
271 hemispheric-wide sea ice variations<sup>40</sup> on these time-scales.

272 We reconstructed winter sea ice extent by diatom assemblage in a temporally

273 well-resolved, nearby sediment record from the northern Scotia Sea (PS69/197-1, Fig.  
274 4E). Within age uncertainties, we observe a close correspondence between  
275 millennial-scale maxima in ACC strength and major winter sea ice retreat intervals  
276 (Fig. 4D, E). Such sizeable reduction of seasonal sea ice is also recorded in other  
277 locations from the Scotia Sea, which revealed seasonal sea ice shifts southward by  $\sim 8^\circ$   
278 latitude, attributed to maxima in regional sea surface temperatures and local insolation  
279 forcing<sup>43</sup>. We propose that Antarctic sea ice extent acted as positive feedback  
280 mechanism on increasing amplitudes in millennial-scale ACC intensity towards the  
281 LGM. Sea ice effectively moderates the momentum transfer of wind-derived energy  
282 into the surface ocean<sup>6,11</sup>, because the air drag over ice and open water fundamentally  
283 differs and scales with the density of sea ice cover. The effect of sea ice on the flow  
284 depends on the ratio of ice floes to patches open water<sup>6,11,58</sup>. In the dynamic Drake  
285 Passage setting, a highly mobile sea ice cover with an optimal concentration (50-90%)  
286 would constitute a strong catalyst between wind and the surface ocean<sup>11,58</sup>. Such optimal  
287 sea ice conditions could increase the air-sea drag coefficient by a factor of two to four<sup>11,58</sup>,  
288 thus yield a strong amplification of glacial millennial-scale variations in SWW forcing on  
289 the ocean surface.



290

291 **Fig. 4. Millennium-scale changes in ACC strength compared to paleoclimatic records over**  
 292 **the last 60 ka.** A, NGRIP oxygen isotope record<sup>53</sup>. B, Bermuda Rise <sup>231</sup>Pa/<sup>230</sup>Th proxy for the  
 293 AMOC strength<sup>47-49</sup>. C, Saturation index as a proxy for reconstructed carbonate saturation changes  
 294 in the South Atlantic<sup>57</sup>. D,  $\overline{SSFS}$  as flow speed proxies for the ACC strength (three-point  
 295 smoothing, this study). E, Relative abundance of diatom winter sea ice indicator *Fragilariopsis*  
 296 *curta* group (*F. curta* + *F. cylindrus*) with three-point smoothing<sup>17,59</sup>. The group abundance >3%  
 297 indicates the presence of winter sea ice<sup>17,59</sup>. F, Synchronized ice-core atmospheric pCO<sub>2</sub><sup>54</sup>. G, δ<sup>18</sup>O  
 298 time series from the EDML ice core<sup>54</sup>. Vertical gray bars mark inferred millennial-scale ACC  
 299 peaks that correspond with millennial scale temperature maxima in Antarctica (AIM) and Heinrich  
 300 events (H) in Greenland.

## 301 **Implications for marine carbon storage and the AMOC**

302 Our records represent significant ACC flow speed variations in the central Drake  
303 Passage on both orbital and millennial timescales. These changes in ACC strength and  
304 Drake Passage through-flow were likely driven by a combination of changes in wind  
305 stress efficiency<sup>9</sup>, oceanic fronts<sup>37</sup>, and sea ice coverage<sup>5,6</sup>. Superimposed on the  
306 long-term changes, the ACC flow speed experienced remarkable millennial-scale  
307 variations. Our results document an enhanced sensitivity of millennial-scale ACC  
308 variations towards the LGM to Southern Hemisphere millennial-scale climate  
309 oscillations. We hypothesize that such increasing amplitudes in millennial-scale ACC  
310 variations approaching the LGM are likely linked to variations of Antarctic sea ice  
311 extent. Changes in millennial-scale ACC strength could have regulated the  
312 Pacific-Atlantic exchange and caused variations of carbonate saturation in the South  
313 Atlantic together with interbasin deep-water evolution<sup>57,60</sup> (Fig. 4B-D). These  
314 processes with wind-driven upwelling<sup>52</sup> and sea-ice condition<sup>17,42,61</sup> (Fig. 4E) might  
315 have modulated the sequestered CO<sub>2</sub> exchange with the atmosphere over millennial  
316 timescales (Fig. 4F).

317 These strong variations of the ACC likely played an important role in shaping  
318 AMOC strength and stability over the past 140 ka. Since a vigorous ACC prevailed  
319 during the last warmer-than-present interglacial<sup>35</sup>, we speculate that under future  
320 warmer climates the ACC would remain similar to or stronger than today. Such a  
321 persistent cold water route return flow into the Atlantic could stabilize the AMOC in  
322 the long-term future, despite the AMOC showing emerging signs of weakening over  
323 the past decades<sup>62</sup>.

324

## 325 **Methods**

326 **Paleomagnetic measurements.** Volume susceptibility on core PS97/085-3 was performed with a  
327 Bartington MS2E sensor and MS2 control unit on a split-core logger in 1 mm intervals and a  
328 sensor amplitude resolution of 10<sup>-5</sup> (see Supplementary Methods). The anisotropy of magnetic  
329 susceptibility (AMS) was determined using an AGICO Multi-Function Kappabridge MFK-1S,  
330 applying a field of 200 mA m<sup>-1</sup> at a frequency of 976 Hz. The orientations of the principle axes of  
331 the AMS ellipsoid, giving information about the status of the magnetic fabric, were provided by

332 the AGICO software ‘Safyr6’. Natural remanent magnetization (NRM) was measured and  
333 stepwise demagnetized with a superconducting 2G Enterprises 755 SRM long-core magnetometer.  
334 Demagnetization was accomplished in 10 steps at AF peak levels of 5, 10, 15, 20, 30, 40, 50, 65,  
335 80, and 100 mT. NRM results were analysed with principle component analysis<sup>63</sup> to determine  
336 direction of the characteristic remanent magnetization (ChRM). An anhysteretic remanent  
337 magnetization (ARM) was imparted using a separate 2G Enterprises 600 AF demagnetizer with  
338 additional coil for a static field. ARMs were stepwise demagnetized with a reduced number of  
339 steps: 10, 20, 30, 40, 50, 65, and 80 mT.

340 **X-ray fluorescence core scanning (XRF-CS).** The sediment core was measured with an  
341 AVAATECH XRF-CS at the Alfred Wegener Institute (AWI), Bremerhaven. XRF-CS data were  
342 collected in 1 cm steps (area 10 x 12 mm) along the core in three runs with 10 kV, 30 kV and 50  
343 kV (see Supplementary Methods).

344 **Age Model.** The age model is based on a combination of radiocarbon dates, paleomagnetic  
345 excursion, correlation of relative paleointensity (RPI) with the RPI stack and tuning from high  
346 resolution XRF-CS ln(Ca/Ti) (Table S1). The high-resolution XRF scanner-derived records of  
347 ln(Ca/Ti) peak area count ratios were used to fine-tune to Antarctic temperature anomalies with  
348 ice core chronology (AICC2012) using the AnalySeries Software<sup>33,64</sup>. Planktonic foraminifera  
349 *Neogloboquadrina pachyderma* were selected for radiocarbon measurements, performed in the  
350 Mini Carbon Dating System (MICADAS) lab at the AWI, Bremerhaven. Bayesian age-depth  
351 modeling program Bacon 2.3<sup>65</sup> was applied to develop an age model based on radiocarbon dates,  
352 paleomagnetic and tuning points (Fig. S2). The error estimate (Table S1) for tuning points and  
353 paleomagnetic tie points was done using mean squared estimate following the method of Grant et  
354 al., (2012)<sup>66</sup> (see Supplementary Methods for <sup>14</sup>C age calibrations).

355 **Grain-size measurements.** A total of 1520 samples were taken in 1 cm intervals from core  
356 (PS97/085-3 for grain-size measurements with a CILAS 1180 L laser diffraction particle-size  
357 analyzer (CILAS, Orleans, France) at the AWI, Sylt. For comparison of different grain-size  
358 measurement methods, 80 samples were measured with a Micromeritics SediGraph 5100 at AWI,  
359 Bremerhaven (see Supplementary Methods and Fig. S6).

360 **Quantification of ice-rafted debris.** Core PS97/085-3 was scanned by a Toshiba Aquilion 64<sup>TM</sup>  
361 computer tomography (CT) at the hospital Klinikum Bremen-Mitte (Bremen, Germany). CT data  
362 were processed with the Amira ZIB edition software<sup>67</sup>. All lithic clasts >1 mm and bioturbation  
363 traces were segmented with the “Threshold” segmentation tool of the Segmentation Editor. Each  
364 analysis considered a core interval of ~1 cm, all results present in volume percentage and number  
365 of clasts per cubic centimeter.

366 **Diatom census.** The sample preparation of permanent mounted slides from core PS67/197-1 for  
367 microscopic diatom census followed the standard procedure established at the AWI<sup>59</sup>. Diatom  
368 species and species groups were identified and counted according to Zielinski and Gersonde  
369 (1997)<sup>68</sup> with a minimum of 400 specimens, at the magnification of ×1000 using a Zeiss  
370 microscope. Relative abundances of sea ice related species *Fragilariopsis curta* and  
371 *Fragilariopsis cylindrus* were combined for estimation of changes in winter sea ice extent<sup>59</sup>.

372

## 373 **Data availability**

374 All relevant data in this paper will be available at PANGAEA Data Publisher.

## 375 Reference

- 376 1 Marshall, J. & Speer, K. Closure of the meridional overturning circulation through Southern  
377 Ocean upwelling. *Nat Geosci* **5**, 171-180, doi: 10.1038/ngeo1391 (2012).
- 378 2 Rintoul, S. R. The global influence of localized dynamics in the Southern Ocean. *Nature* **558**,  
379 209-218, doi: 10.1038/s41586-018-0182-3 (2018).
- 380 3 Sigman, D. M. & Boyle, E. A. Glacial/interglacial variations in atmospheric carbon dioxide.  
381 *Nature* **407**, 859, doi:10.1038/35038000 (2000).
- 382 4 Gottschalk, J. *et al.* Biological and physical controls in the Southern Ocean on past  
383 millennial-scale atmospheric CO<sub>2</sub> changes. *Nature Communications* **7**, 11539, doi:  
384 10.1038/ncomms11539 (2016).
- 385 5 Lamy, F. *et al.* Glacial reduction and millennial-scale variations in Drake Passage throughflow.  
386 *Proceedings of the National Academy of Sciences* **112**, 13496-13501, doi:  
387 10.1073/pnas.1509203112 (2015).
- 388 6 McCave, I., Crowhurst, S., Kuhn, G., Hillenbrand, C. & Meredith, M. Minimal change in  
389 Antarctic Circumpolar Current flow speed between the last glacial and Holocene. *Nat Geosci*  
390 **7**, 113-116, doi: 10.1038/ngeo2037 (2014).
- 391 7 Roberts, J. *et al.* Deglacial changes in flow and frontal structure through the Drake Passage.  
392 *Earth Planet Sc Lett* **474**, 397-408, doi: 10.1016/j.epsl.2017.07.004 (2017).
- 393 8 Toyos, M. H. *et al.* Antarctic Circumpolar Current dynamics at the Pacific entrance to the  
394 Drake Passage over the past 1.3 million years. *Paleoceanography and Paleoclimatology* **35**,  
395 e2019PA003773, doi: 10.1029/2019pa003773 (2020).
- 396 9 Toggweiler, J. R., Russell, J. L. & Carson, S. R. Midlatitude westerlies, atmospheric CO<sub>2</sub>, and  
397 climate change during the ice ages. *Paleoceanography* **21**, doi: 10.1029/2005pa001154  
398 (2006).
- 399 10 Shi, J.-R., Talley, L. D., Xie, S.-P., Liu, W. & Gille, S. T. Effects of Buoyancy and Wind  
400 Forcing on Southern Ocean Climate Change. *J Climate*, 1-53, doi: 10.1175/jcli-d-19-0877.1  
401 (2020).
- 402 11 Martin, T., Steele, M. & Zhang, J. Seasonality and long-term trend of Arctic Ocean surface  
403 stress in a model. *Journal of Geophysical Research: Oceans* **119**, 1723-1738, doi:  
404 10.1002/2013jc009425 (2014).
- 405 12 Orsi, A. H., Whitworth III, T. & Nowlin Jr, W. D. On the meridional extent and fronts of the  
406 Antarctic Circumpolar Current. *Deep Sea Research Part I: Oceanographic Research Papers*  
407 **42**, 641-673, doi: 10.1016/0967-0637(95)00021-W (1995).
- 408 13 Rintoul, S. R. South Atlantic interbasin exchange. *Journal of Geophysical Research: Oceans*  
409 **96**, 2675-2692, doi: 10.1029/90jc02422 (1991).
- 410 14 Gordon, A. L. Interocean exchange of thermocline water. *Journal of Geophysical Research:*  
411 *Oceans* **91**, 5037-5046, doi: 10.1029/JC091iC04p05037 (1986).
- 412 15 Knorr, G. & Lohmann, G. Southern Ocean origin for the resumption of Atlantic thermohaline  
413 circulation during deglaciation. *Nature* **424**, 532, doi: 10.1038/nature01855 (2003).
- 414 16 Beal, L. M., De Ruijter, W. P. M., Biastoch, A., Zahn, R. & Grp, S. W. I. W. On the role of the  
415 Agulhas system in ocean circulation and climate. *Nature* **472**, 429-436, doi:  
416 10.1038/nature09983 (2011).
- 417 17 Xiao, W., Esper, O. & Gersonde, R. Last Glacial - Holocene climate variability in the Atlantic

418 sector of the Southern Ocean. *Quaternary Sci Rev* **135**, 115-137, doi:  
419 10.1016/j.quascirev.2016.01.023 (2016).

420 18 Xiao, W. *et al.* Constraining the dating of late Quaternary marine sediment records from the  
421 Scotia Sea (Southern Ocean). *Quaternary Geochronology* **31**, 97-118, doi:  
422 10.1016/j.quageo.2015.11.003 (2016).

423 19 Chaigneau, A. & Pizarro, O. Surface circulation and fronts of the South Pacific Ocean, east of  
424 120° W. *Geophys Res Lett* **32**, doi: 10.1029/2004gl022070 (2005).

425 20 Drouin, K. L. & Lozier, M. S. The Surface Pathways of the South Atlantic: Revisiting the  
426 Cold and Warm Water Routes Using Observational Data. *Journal of Geophysical Research:  
427 Oceans* **124**, 7082-7103, doi: 10.1029/2019jc015267 (2019).

428 21 Hernández-Molina, F. J., Larter, R. D. & Maldonado, A. Neogene to Quaternary stratigraphic  
429 evolution of the Antarctic Peninsula, Pacific Margin offshore of Adelaide Island: Transitions  
430 from a non-glacial, through glacially-influenced to a fully glacial state. *Global Planet Change*  
431 **156**, 80-111, doi: 10.1016/j.gloplacha.2017.07.002 (2017).

432 22 Comiso, J. C. in *Sea Ice: An Introduction to Its Physics, Chemistry, Biology and Geology*  
433 (ed G.S. Thomas D.N; Diekmann) Ch. 4, 112-142 (2003).

434 23 McCave, I. N. & Hall, I. R. Size sorting in marine muds: Processes, pitfalls, and prospects for  
435 paleoflow-speed proxies. *Geochem Geophys Geosy* **7**, doi: 10.1029/2006gc001284 (2006).

436 24 McCave, I. N., Manighetti, B. & Robinson, S. G. Sortable silt and fine sediment  
437 size/composition slicing: parameters for palaeocurrent speed and palaeoceanography.  
438 *Paleoceanography* **10**, 593-610, doi: 10.1029/94PA03039 (1995).

439 25 Wu, S. *et al.* Surface sediment characteristics related to provenance and ocean circulation in  
440 the Drake Passage sector of the Southern Ocean. *Deep Sea Research Part I: Oceanographic  
441 Research Papers* **154**, 103135, doi: 10.1016/j.dsr.2019.103135 (2019).

442 26 Donohue, K., Tracey, K., Watts, D., Chidichimo, M. & Chereskin, T. Mean Antarctic  
443 Circumpolar Current transport measured in Drake Passage. *Geophys Res Lett* **43**, doi:  
444 10.1002/2016GL070319 (2016).

445 27 McCave, I. N. & Andrews, J. T. Distinguishing current effects in sediments delivered to the  
446 ocean by ice. I. Principles, methods and examples. *Quaternary Sci Rev* **212**, 92-107, doi:  
447 10.1016/j.quascirev.2019.03.031 (2019).

448 28 Fralick, P. W. & Kronberg, B. I. Geochemical discrimination of clastic sedimentary rock  
449 sources. *Sediment Geol* **113**, 111-124, doi: 10.1016/S0037-0738(97)00049-3 (1997).

450 29 Chen, J. *et al.* Zr/Rb ratio in the Chinese loess sequences and its implication for changes in the  
451 East Asian winter monsoon strength. *Geochim Cosmochim Ac* **70**, 1471-1482, doi:  
452 10.1016/j.gca.2005.11.029 (2006).

453 30 Dypvik, H. & Harris, N. B. Geochemical facies analysis of fine-grained siliciclastics using  
454 Th/U, Zr/Rb and (Zr+Rb)/Sr ratios. *Chemical Geology* **181**, 131-146, doi:  
455 10.1016/S0009-2541(01)00278-9 (2001).

456 31 Walter, H., Hegner, E., Diekmann, B. & Kuhn, G. Provenance and transport of terrigenous  
457 sediment in the South Atlantic Ocean and their relations to glacial and interglacial cycles: Nd  
458 and Sr isotopic evidence. *Geochim Cosmochim Ac* **64**, 3813-3827, doi:  
459 10.1016/S0016-7037(00)00476-2 (2000).

460 32 Diekmann, B. *et al.* Terrigenous sediment supply in the Scotia Sea (Southern Ocean): response  
461 to Late Quaternary ice dynamics in Patagonia and on the Antarctic Peninsula. *Palaeogeogr*

462 *Palaeocl* **162**, 357-387, doi: 10.1016/S0031-0182(00)00138-3 (2000).

463 33 Jouzel, J. *et al.* Orbital and millennial Antarctic climate variability over the past 800,000 years.  
464 *Science* **317**, 793-796, doi: 10.1126/science.1141038 (2007).

465 34 Veres, D. *et al.* The Antarctic ice core chronology (AICC2012): an optimized multi-parameter  
466 and multi-site dating approach for the last 120 thousand years. *Clim Past* **9**, 1733-1748, doi:  
467 10.5194/cp-9-1733-2013 (2013).

468 35 Shackleton, S. *et al.* Global ocean heat content in the Last Interglacial. *Nat Geosci* **13**, 77-81,  
469 doi: 10.1038/s41561-019-0498-0 (2020).

470 36 Koenig, Z., Provost, C., Ferrari, R., Sennéchaël, N. & Rio, M.-H. Volume transport of the  
471 Antarctic Circumpolar Current: Production and validation of a 20 year long time series  
472 obtained from in situ and satellite observations. *Journal of Geophysical Research: Oceans* **119**,  
473 5407-5433, doi: 10.1002/2014JC009966 (2014).

474 37 Gersonde, R., Crosta, X., Abelmann, A. & Armand, L. Sea-surface temperature and sea ice  
475 distribution of the Southern Ocean at the EPILOG Last Glacial Maximum—a  
476 circum-Antarctic view based on siliceous microfossil records. *Quaternary Sci Rev* **24**,  
477 869-896, doi: 10.1016/j.quascirev.2004.07.015 (2005).

478 38 Kohfeld, K. E. *et al.* Southern Hemisphere westerly wind changes during the Last Glacial  
479 Maximum: paleo-data synthesis. *Quaternary Sci Rev* **68**, 76-95, doi:  
480 10.1016/j.quascirev.2013.01.017 (2013).

481 39 Sime, L. C. *et al.* Southern Hemisphere westerly wind changes during the Last Glacial  
482 Maximum: model-data comparison. *Quaternary Sci Rev* **64**, 104-120, doi:  
483 10.1016/j.quascirev.2012.12.008 (2013).

484 40 Fischer, H. *et al.* Reconstruction of millennial changes in dust emission, transport and regional  
485 sea ice coverage using the deep EPICA ice cores from the Atlantic and Indian Ocean sector of  
486 Antarctica. *Earth Planet Sc Lett* **260**, 340-354, doi: 10.1016/j.epsl.2007.06.014 (2007).

487 41 Levine, J. G., Yang, X., Jones, A. E. & Wolff, E. W. Sea salt as an ice core proxy for past sea  
488 ice extent: A process-based model study. *Journal of Geophysical Research: Atmospheres* **119**,  
489 5737-5756, doi: 10.1002/2013jd020925 (2014).

490 42 Ferrari, R. *et al.* Antarctic sea ice control on ocean circulation in present and glacial climates.  
491 *Proceedings of the National Academy of Sciences* **111**, 8753-8758, doi:  
492 10.1073/pnas.1323922111 (2014).

493 43 Collins, L. G., Pike, J., Allen, C. S. & Hodgson, D. A. High-resolution reconstruction of  
494 southwest Atlantic sea-ice and its role in the carbon cycle during marine isotope stages 3 and 2.  
495 *Paleoceanography* **27**, doi: 10.1029/2011pa002264 (2012).

496 44 Markle, B. R., Steig, E. J., Roe, G. H., Winckler, G. & McConnell, J. R. Concomitant  
497 variability in high-latitude aerosols, water isotopes and the hydrologic cycle. *Nat Geosci* **11**,  
498 853-859, doi: 10.1038/s41561-018-0210-9 (2018).

499 45 Christo, B. & Andreas, S. Southern Ocean control of glacial AMOC stability and  
500 Dansgaard-Oeschger interstadial duration. *Paleoceanography* **30**, 1595-1612, doi:  
501 10.1002/2015PA002795 (2015).

502 46 Peeters, F. J. *et al.* Vigorous exchange between the Indian and Atlantic oceans at the end of the  
503 past five glacial periods. *Nature* **430**, 661, doi: 10.1038/nature02785 (2004).

504 47 Bohm, E. *et al.* Strong and deep Atlantic meridional overturning circulation during the last  
505 glacial cycle. *Nature* **517**, 73-76, doi: 10.1038/nature14059 (2015).

506 48 Henry, L. G. *et al.* North Atlantic ocean circulation and abrupt climate change during the last  
507 glaciation. *Science* **353**, 470-474, doi: 10.1126/science.aaf5529 (2016).

508 49 McManus, J. F., Francois, R., Gherardi, J. M., Keigwin, L. D. & Brown-Leger, S. Collapse  
509 and rapid resumption of Atlantic meridional circulation linked to deglacial climate changes.  
510 *Nature* **428**, 834, doi: 10.1038/nature02494 (2004).

511 50 Caley, T. *et al.* Quantitative estimate of the paleo-Agulhas leakage. *Geophys Res Lett* **41**,  
512 1238-1246, doi: 10.1002/2014GL059278 (2014).

513 51 Meredith, M. P. *et al.* Sustained monitoring of the Southern Ocean at Drake Passage: Past  
514 achievements and future priorities. *Reviews of Geophysics* **49**, doi: 10.1029/2010RG000348  
515 (2011).

516 52 Anderson, R. F. *et al.* Wind-driven upwelling in the Southern Ocean and the deglacial rise in  
517 atmospheric CO<sub>2</sub>. *Science* **323**, 1443-1448, doi: 10.1126/science.1167441 (2009).

518 53 Andersen, K. K. *et al.* High-resolution record of Northern Hemisphere climate extending into  
519 the last interglacial period. *Nature* **431**, 147-151, doi: 10.1038/nature02805 (2004).

520 54 EPICA Community Members. One-to-one coupling of glacial climate variability in Greenland  
521 and Antarctica. *Nature* **444**, 195-198, doi: 10.1038/nature05301 (2006).

522 55 Bond, G. *et al.* Evidence for massive discharges of icebergs into the North Atlantic ocean  
523 during the last glacial period. *Nature* **360**, 245-249, doi: 10.1038/360245a0 (1992).

524 56 Caniupan, M. *et al.* Millennial-scale sea surface temperature and Patagonian Ice Sheet  
525 changes off southernmost Chile (53 degrees S) over the past similar to 60 kyr.  
526 *Paleoceanography* **26**, doi: 10.1029/2010pa002049 (2011).

527 57 Gottschalk, J. *et al.* Abrupt changes in the southern extent of North Atlantic Deep Water  
528 during Dansgaard–Oeschger events. *Nat Geosci* **8**, 950, doi: 10.1038/ngeo2558 (2015).

529 58 Lüpkes, C., Gryanik, V. M., Hartmann, J. & Andreas, E. L. A parametrization, based on sea ice  
530 morphology, of the neutral atmospheric drag coefficients for weather prediction and climate  
531 models. *Journal of Geophysical Research: Atmospheres* **117**, doi:10.1029/2012jd017630  
532 (2012).

533 59 Gersonde, R. & Zielinski, U. The reconstruction of late Quaternary Antarctic sea-ice  
534 distribution—the use of diatoms as a proxy for sea-ice. *Palaeogeography, Palaeoclimatology,*  
535 *Palaeoecology* **162**, 263-286, doi: 10.1016/S0031-0182(00)00131-0 (2000).

536 60 Yu, J. *et al.* Last glacial atmospheric CO<sub>2</sub> decline due to widespread Pacific deep-water  
537 expansion. *Nat Geosci*, doi: 10.1038/s41561-020-0610-5 (2020).

538 61 Stein, K., Timmermann, A., Kwon, E. Y. & Friedrich, T. Timing and magnitude of Southern  
539 Ocean sea ice/carbon cycle feedbacks. *Proceedings of the National Academy of Sciences*,  
540 201908670, doi:10.1073/pnas.1908670117 (2020).

541 62 Srokosz, M. & Bryden, H. Observing the Atlantic Meridional Overturning Circulation yields a  
542 decade of inevitable surprises. *Science* **348**, 1255575, doi: 10.1126/science.1255575 (2015).

543 63 Kirschvink, J. L. The least-squares line and plane and the analysis of palaeomagnetic data.  
544 *Geophysical Journal International* **62**, 699-718, doi: 10.1111/j.1365-246X.1980.tb02601.x  
545 (1980).

546 64 Paillard, D., Labeyrie, L. & Yiou, P. Macintosh Program performs time-series analysis. *Eos,*  
547 *Transactions American Geophysical Union* **77**, 379-379, doi: 10.1029/96eo00259 (1996).

548 65 Blaauw, M. & Christen, J. A. Flexible paleoclimate age-depth models using an autoregressive  
549 gamma process. *Bayesian analysis* **6**, 457-474, doi: 10.1214/11-BA618 (2011).

550 66 Grant, K. M. *et al.* Rapid coupling between ice volume and polar temperature over the past  
551 150,000 years. *Nature* **491**, 744-747, doi: 10.1038/nature11593 (2012).  
552 67 Stalling, D., Westerhoff, M. & Hege, H.-C. Amira: A highly interactive system for visual data  
553 analysis. *The visualization handbook* **38**, 749-767 (2005).  
554 68 Zielinski, U. & Gersonde, R. Diatom distribution in Southern Ocean surface sediments  
555 (Atlantic sector): implications for paleoenvironmental reconstructions. *Palaeogeography,*  
556 *Palaeoclimatology, Palaeoecology* **129**, 213-250, doi: 10.1016/S0031-0182(96)00130-7  
557 (1997).  
558

### 559 **Acknowledgements**

560 We thank the captain, crew and scientific party of RV Polarstern Expedition PS97 for their professional  
561 help in retrieving the sediment samples. We also thank C. Lange, X. Gong and A. C. Ravelo for  
562 discussions. We sincerely thank S. Wiebe and R. Fröhling-Teichert at the Alfred Wegener Institute  
563 (AWI) for technical assistance in sample preparation, grain-size measurements and XRF scans.  
564 Klinikum Bremen-Mitte and A.-J. Lemke and C. Tiemann, Gesundheit Nord Bremen, are gratefully  
565 acknowledge for providing facilities and supporting the computed tomography measurements. This  
566 study was supported by the AWI Helmholtz Centre for Polar and Marine Research research programme  
567 “Polar Regions and Coasts in the changing Earth System” (PACES II) and the China Scholarship  
568 Council (CSC No. 201604910671).

569

### 570 **Author contributions**

571 S.Z.W. together with L.L.J., F.L. and G.K. led the research. S.Z.W. carried out high-resolution  
572 grain-size measurements and analyzed the data. L.D. performed additional sortable silt measurements.  
573 J.T. led CT scanning and processed data with S.Z.W. . H.W.A. and G.K. contributed XRF core scanning  
574 and magnetic susceptibility data. X.F.Z. and J.B.L carried out magnetic property measurements. L.L.J.  
575 contributed <sup>14</sup>C data. H.W.A., N.N., F.L. and S.Z.W. generated age model. W.S.X. carried out diatom  
576 counts for sea ice reconstruction. X.Z. helped shape the initial concept and contribute to data  
577 interpretation. S.Z.W. wrote the manuscript with contribution from L.L.J., F.L. and G.K. All the  
578 co-authors contributed to the interpretation of the results and provided inputs to the final version.

579

### 580 **Competing interests**

581 The authors declare no competing interests.

# Figures

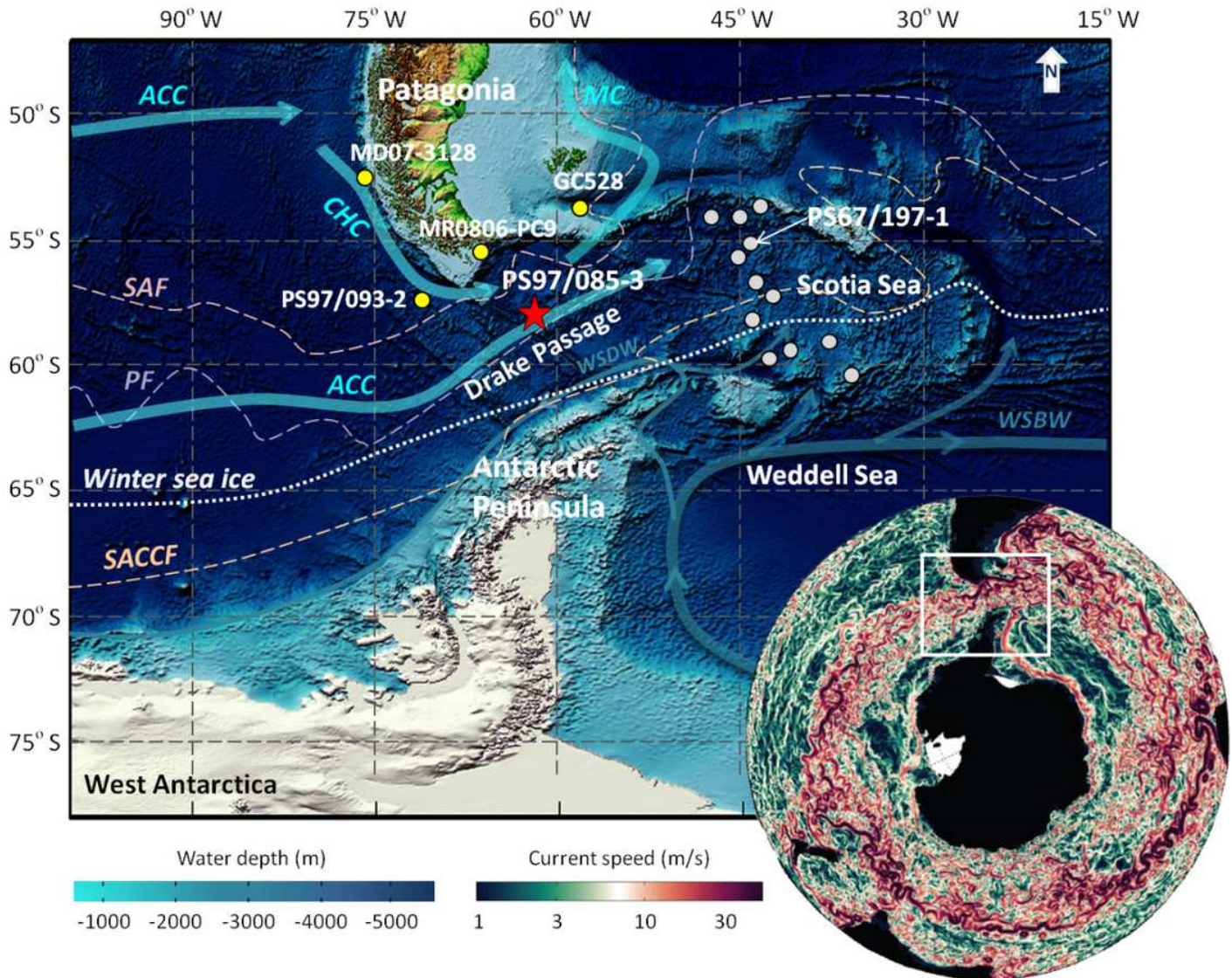


**Figure 1**

Core PS97/085-3 is located in the central Drake Passage (red star), ~20 nm north of the Polar Front (see Supplementary Fig. S1). Yellow dots mark sediment cores in north of the Subantarctic Front<sup>5,7,8</sup>. Grey dots indicate Scotia Sea transect cores south of the Polar Front<sup>6</sup>. Core PS67/197-1 in the Scotia Sea is sensitive to changes in winter sea ice extent<sup>17</sup>. Light blue arrows show the Antarctic Circumpolar Current (ACC), the Cape Horn Current (CHC)<sup>19</sup> and Malvinas Current (MC)<sup>20</sup>, while dark green-blue arrows are Weddell Sea Bottom Water (WSBW, thick) and Weddell Sea Deep Water (WSDW, thin) flows<sup>21</sup>. White dotted line is average modern winter sea ice edge<sup>22</sup>. Dashed lines are the Subantarctic Front (SAF, pink), Polar Front (PF, purple) and the Southern Antarctic Circumpolar Current Front (SACCF, orange)<sup>12</sup>. The right bottom insert map shows study area inside the white box and current speed in the Southern Ocean, with warmer red colors representing higher current speeds<sup>2</sup> adapted from Wu et al. (2019).

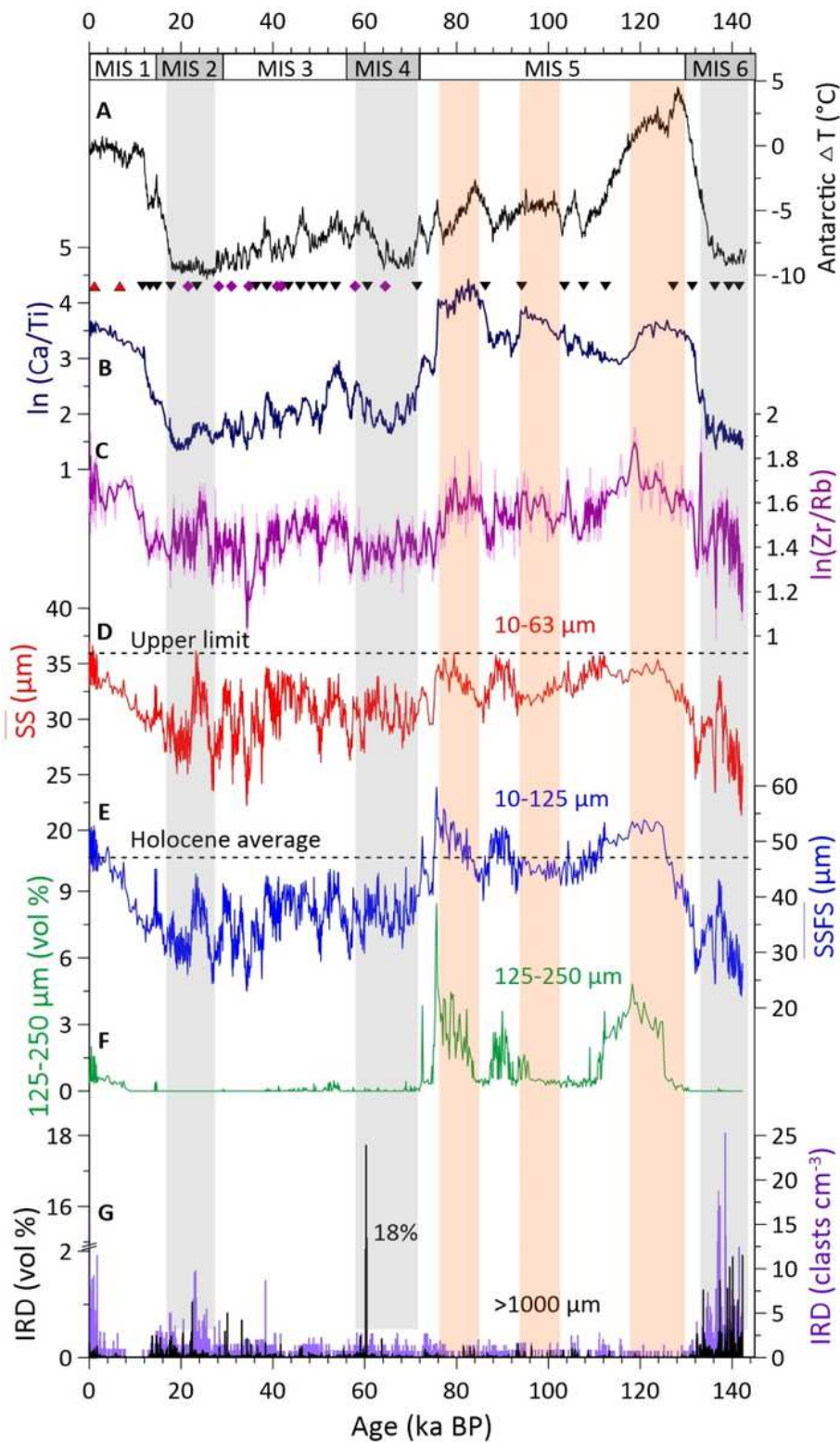


**Figure 2**

Reconstructed changes in ACC intensity and compared with Southern Hemisphere temperature signature. A, Antarctic temperature changes from the European Project for Ice Coring in Antarctica (EPICA) Dome C ice core<sup>33</sup>. B, High-resolution XRF scanner-derived records of  $\ln(\text{Ca}/\text{Ti})$  (peak area count ratios) were applied to fine-tune to the Antarctic temperature anomalies together with radiocarbon dates, relative paleo-intensity and paleomagnetic excursions age control points from core PS97/085-3 (see

Supplementary Methods, Fig. S2; S3). C, XRF-derived Zr/Rb variations indicate changes in sediment grain-size fractions. D, Mean sortable silt grain size ((SS)  $\bar{x}$ , 10-63  $\mu\text{m}$ ) reaches up its limit under high flow speeds. E, Mean grain size of sortable silt and fine sand ((SSFS)  $\bar{x}$ , 10-125  $\mu\text{m}$ ) was used as the ACC strength proxy in this study. F, Coarse sand fraction (125-250  $\mu\text{m}$ ), mainly in interglacials, inferring high current speeds highlights the extension of the sorting effect to coarser grain sizes. G, Ice-rafted debris (IRD) defined by larger than 1 mm grain size from X-ray computed topography scan (CT, see Supplementary Methods). Vertical gray bars mark inferred glacial periods and pink bars inferred the sub-interglacial during Marine Isotope Stage (MIS) 5.

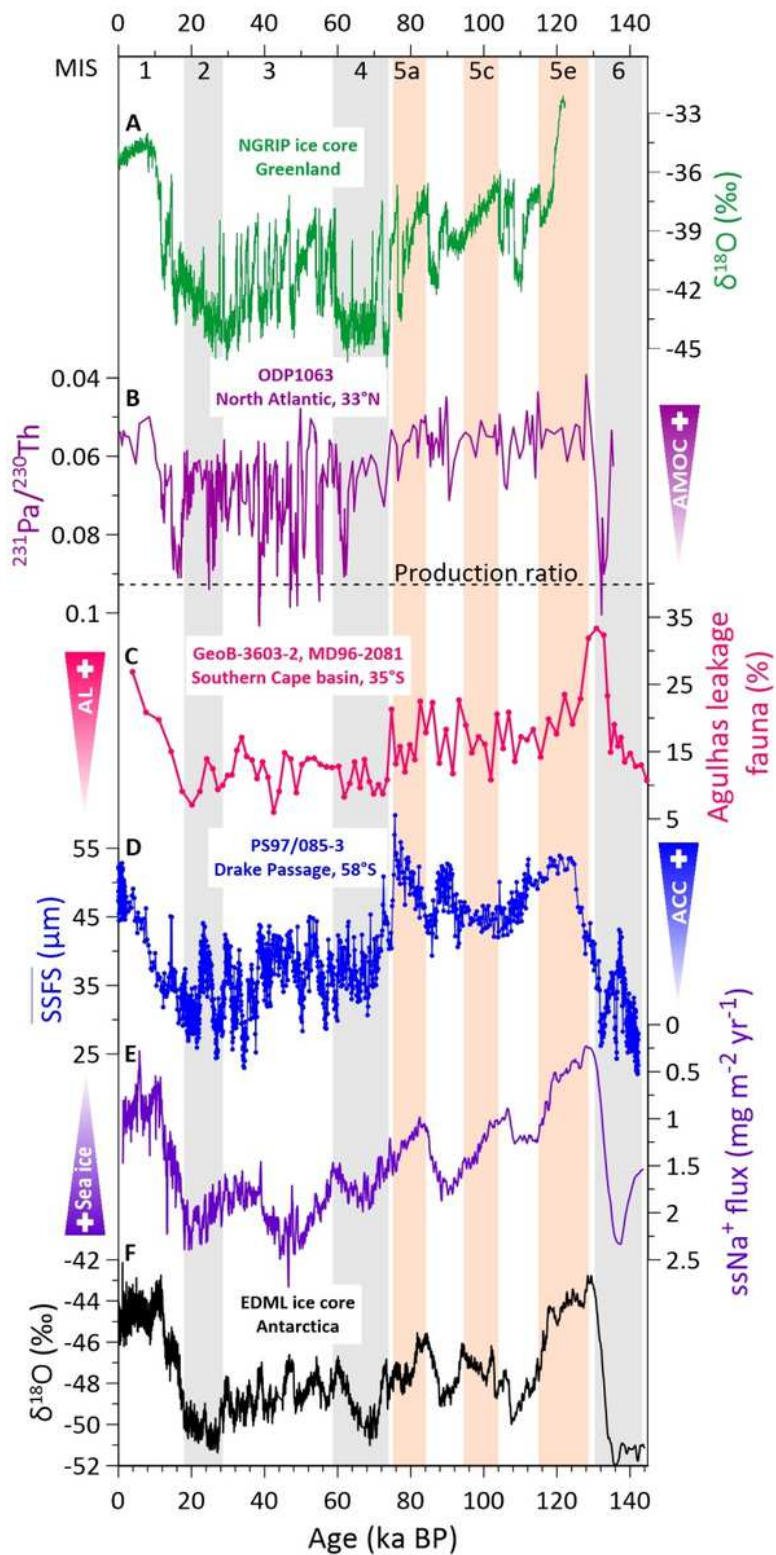


**Figure 3**

Reconstructed changes in ACC strength compared with paleoclimatic records over the past 140 ka. A, Oxygen isotope record from North Greenland Ice Core Project (NGRIP,  $\delta^{18}\text{O}$  vs. VSMOW)<sup>53</sup>. B, Bermuda Rise  $^{231}\text{Pa}/^{230}\text{Th}$  data<sup>47-49</sup>, indicating the AMOC strength. Dashed line is production ratio ( $^{231}\text{Pa}/^{230}\text{Th} = 0.093$ ), suggesting no transport. C, planktic foraminiferal fauna reflect the intensity of the Agulhas leakage<sup>46</sup>. D, (SSFS)  $\bar{x}$  as a flow-speed proxy for the ACC strength (blue, this study). E, Sea

salt sodium (ssNa) flux from EPICA Dronning Maud Land (EDML) ice core, a proxy for sea ice, smoothed with a three-points running mean<sup>40</sup>. F, Oxygen isotope record from the EDML ice core<sup>54</sup>. Vertical gray bars mark glacial periods and pink bars mark the warm stages during MIS 5.

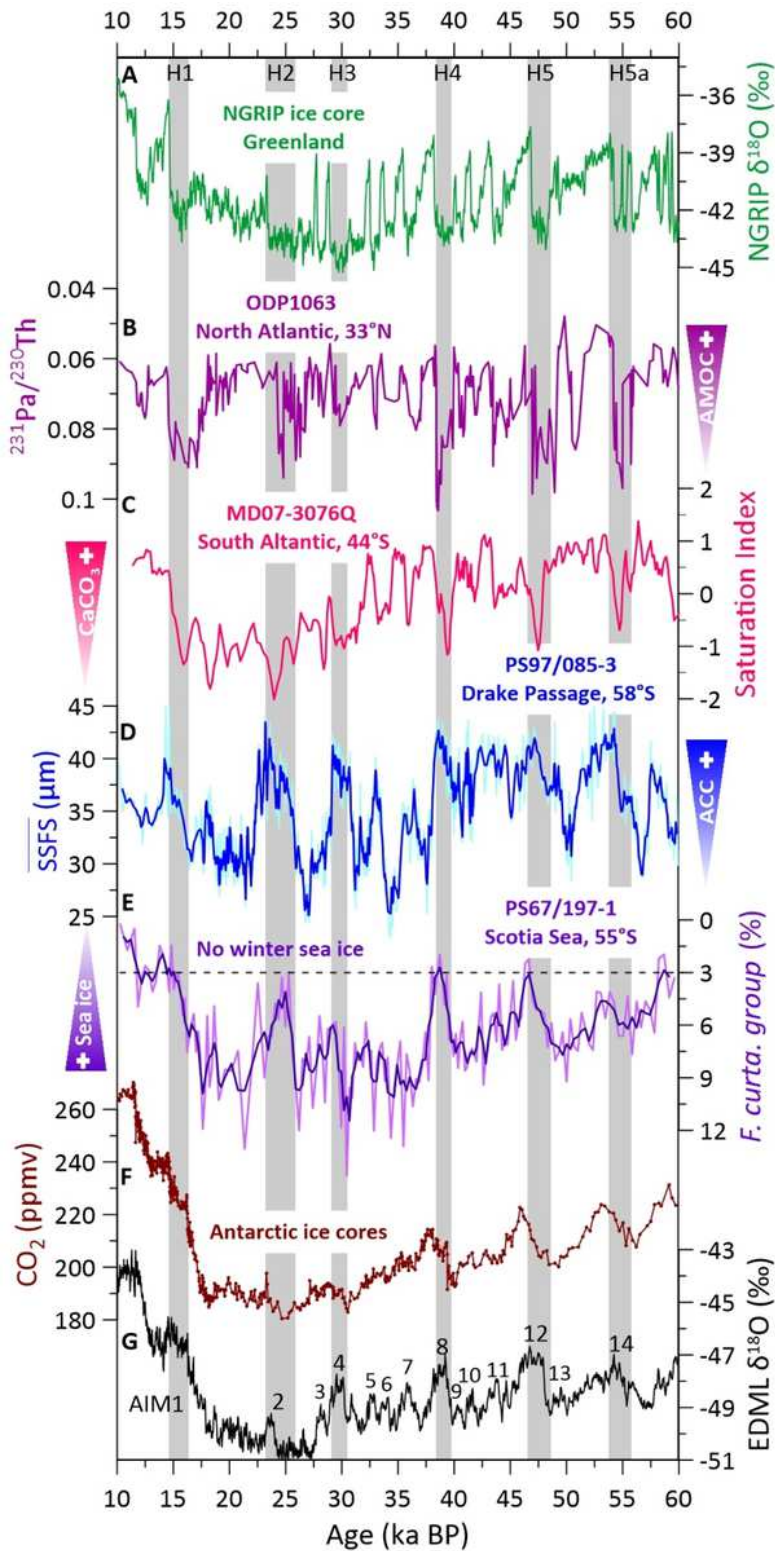


**Figure 4**

Millennium-scale changes in ACC strength compared to paleoclimatic records over the last 60 ka. A, NGRIP oxygen isotope record<sup>53</sup>. B, Bermuda Rise  $^{231}\text{Pa}/^{230}\text{Th}$  proxy for the AMOC strength<sup>47-49</sup>. C,

Saturation index as a proxy for reconstructed carbonate saturation changes in the South Atlantic<sup>57</sup>. D, (SSFS)  $\delta$  as flow speed proxies for the ACC strength (three-point smoothing, this study). E, Relative abundance of diatom winter sea ice indicator *Fragilariopsis curta* group (*F. curta* + *F. cylindrus*) with three-point smoothing<sup>17,59</sup>. The group abundance >3% indicates the presence of winter sea ice<sup>17,59</sup>. F, Synchronized ice-core atmospheric pCO<sub>2</sub><sup>54</sup>. G,  $\delta$ 18O time series from the EDML ice core<sup>54</sup>. Vertical gray bars mark inferred millennial-scale ACC peaks that correspond with millennial scale temperature maxima in Antarctica (AIM) and Heinrich events (H) in Greenland.

## Supplementary Files

This is a list of supplementary files associated with this preprint. Click to download.

- [SupportingInformation.docx](#)